Commun. Theor. Phys. **77** (2025) 105402 (13pp) https://doi.org/10.1088/1572-9494/add255
CSTR: 32041.14.CTPadd255

Accretion disk images around dilatonic black holes in dilaton-massive gravity

Faizah D Alanazi[1], Shahid Chaudhary[2,3,*], Muhammad Danish Sultan[4], Ali M Mubaraki[5], Saad Althobaiti[6], Awatef Abidi[7], Ahmadjon Abdujabbarov[8,9] and Asifa Ashraf[10]

[1] Department of Mathematics, College of Science, Northern Border University, Arar, Saudi Arabia
[2] Department of Natural Sciences and Humanities, University of Engineering and Technology Lahore, New Campus, Pakistan
[3] Research Center of Astrophysics and Cosmology, Khazar University, Baku, AZ1096, 41 Mehseti Street, Azerbaijan
[4] Department of Physics, Durham University, United Kingdom
[5] Department of Mathematics and Statistics, College of Science, Taif University, PO Box 11099, Taif 21944, Saudi Arabia
[6] Department of Science and Technology, University College Ranyah, Taif University, Ranyan, 21975, Saudi Arabia
[7] Physics Department, College of Sciences Abha, King Khalid University, Saudi Arabia
[8] New Uzbekistan University, Movarounnahr street 1, Tashkent 100000, Uzbekistan
[9] Shahrisabz State Pedagogical Institute, Shahrisabz Str. 10, Shahrisabz 181301, Uzbekistan
[10] School of Mathematical Sciences, Zhejiang Normal University, Jinhua, Zhejiang 321004, China

E-mail: Faizah.alanazi@nbu.edu.sa, shahidpeak00735@gmail.com, drshahid.ch@uet.edu.pk, alimobarki@tu.edu.sa, snthobaiti@tu.edu.sa, mianyasir319@gmail.com, ahmadjon@astrin.uz and asifamustafa3828@gmail.com

Received 8 October 2024, revised 18 March 2025
Accepted for publication 16 April 2025
Published 25 June 2025

Abstract

We consider the recently developed black hole in massive Einstein-dilaton gravity including the coupling of the dilaton scalar field to massive graviton terms. This model has different horizon structures such as event horizons and inner horizons depending on the values of certain parameters. These variations influence how the black hole interacts with its surroundings. We utilize the well-known Novikov–Thorne model to investigate the thin accretion disks into this interesting model. Our research shows a crucial correlation between the dynamics of the accretion disk and the parameters of dilatonic black holes in dilaton-massive gravity. We observe that dilaton-massive gravity leads to significant contraction and outward expansion. We offer a detailed analysis of accretion by examining both direct and secondary images at various radial distances and observation angles.

Keywords: dilatonic black holes, massive gravity, images and accretion disks

1. Introduction

The existence of accretion disks around black holes (BHs) is well-supported by a wealth of observational data. Significant advancements were made with the contributions of the Event Horizon Telescope (EHT), providing unparalleled views into the structures of BHs. One of its most notable outcomes was the famous image of the supermassive BH in M87*, revealing a photon ring encircled by an accretion disk [1]. This behavior is also seen in the supermassive Sgr A* BH in the Milky Way, where it has been confirmed that there is a disk close to the BH [2]. The 1970s marked the beginning of the development of accretion disk models, including the well-known Sunyaev model. This model describes a disk by defining its properties [3]. Afterward, Luminet examined the primary/secondary images of an accretion disk surrounding a Schwarzschild BH using a semi-analytical method [4]. Later, Laor created a technique to compute the line profiles released by disks

* Author to whom any correspondence should be addressed.

highlighting the flux that is primarily produced by the disk's inner region, causing the line peak to blue shift [5]. The accretion disks in different gravity models have increased considerable intensions [6–10]. Guo *et al* carried out a methodical investigation of the photon ring and thin accretion disk characteristics in charged BHs [11, 12]. Their research highlights the complex interplay between accretion disk characteristics of BHs. Recent studies have explored accretion disks around regular BHs. Yergali *et al* [13] examined the properties of accretion disks surrounding regular BH solutions derived from non-linear electrodynamics. Boshkayev, Kuantay, *et al* [14] analyzed the luminosity of accretion disks around rotating regular BHs.

Although many observations can be satisfactorily explained by Einstein's general relativity (GR), there is a need to explore alternative explanations because of the origin of the Universe's acceleration [15, 16] and CMB radiation [17]. Dilaton gravity is a theory that arises from the low-energy limit of string theory as an alternative to general relativity [18]. In string theory, the dilaton field has an important contribution when combined with other gauge fields and gravity. Numerous efforts have been undertaken to explore this theory. For instance, [19, 20] demonstrated that curvature singularities at finite radii result from the dilaton field changing structure of BHs. In addition to changing the asymptotic behavior of the solutions, the dilaton is the generalization of the cosmological constant. The BH solutions by the combination of different dilaton potentials have been examined [21]. Furthermore, scalar-tensor generalizations of general relativity with the dilaton scalar field are investigated in [22, 23]. Einstein-dilaton–Gauss–Bonnet (EdGB) gravity, was thoroughly investigated in [24]. It was discovered that the scalar dilaton, whose charge is represented in terms of the mass of the BH, functions as secondary hair. Afterward, wormholes [25], rapidly rotating neutron stars [26], rotating BHs [27], and BHs in different dimensions were all studied using EdGB gravity [28, 29].

Spin-2 graviton is the main concept in a unique theory that describes the gravity field from the standpoint of contemporary particle physics [30]. Giving the graviton mass allows for the simple alteration of massive gravity. Fierz and Pauli [31] developed a linear theory of massive gravity (MG). However, at the non-linear level, this theory approaches the ghost problem [32]. In [33] it was established that the ghost-free massive theory known as dRGT MG. The thermodynamics of (charged) BH solutions in asymptotically AdS spacetime were studied in dRGT MG [34–36]. It was discovered that the graviton mass-related potential coefficients function similarly to charge in thermodynamic phase space. In MG, additional BH solutions were also investigated [37–39]. Additionally, dilatonic BHs have been proposed [40–43]. By considering the non-minimal coupling of the dilaton field to the graviton and derive analytical solutions for charged dilatonic BHs with massive dilaton gravity. Recently, significant progress has been made in the study of dilatonic BHs. Abishev *et al* [44] explored dyon-like BH solutions within a model featuring two Abelian gauge fields. Malybayev *et al* [45] investigated quasinormal modes in the field of a dyon-like dilatonic BH, while Boshkayev *et al* [46] analyzed geodesics for double-charged dilatonic BHs.

The presence of a dilaton field and BH charge introduces deviations in the spacetime geometry compared to uncharged BHs or those without a dilaton. Studying accretion disks in this context can reveal how the dilaton and charge affect the dynamics of matter around the BH, influencing aspects such as the disk structure, energy dissipation, and emitted radiation. These deviations are crucial for distinguishing dilatonic BHs from those predicted by general relativity. Analyzing accretion around charged dilatonic BHs helps model and predict the observational signatures of these objects. Understanding the behavior of matter in extreme gravitational environments influenced by dilaton and MG components aids in explaining various astrophysical processes more accurately. Charged dilatonic BHs exhibit unique thermodynamic properties, such as modified entropy and temperature relations. Studying accretion disks can further our understanding of the thermodynamic behavior of BHs in dilaton-MG, providing insight into how BHs exchange energy and mass with their surroundings. This is particularly relevant in the study of BH thermodynamics and entropy bounds. With advancements in astronomical instruments, such as the Event Horizon Telescope (EHT), it is becoming increasingly possible to observe the environment around BHs with greater precision. Studying accretion disks around charged dilatonic BHs helps predict observable features, such as the photon ring, spectral lines, and light curves, that can serve as signatures for identifying dilatonic BHs in future observations.

The paper is organized as follows, in section 2, we study the solution of charged dilatonic BH. In section 3, we investigate an analysis of the accretion disk of dilatonic BHs in dilaton-MG. Finally, in section 4, we summarize our results in the conclusion.

2. Dilatonic black holes in dilaton-massive gravity

In four-dimensional spacetime, the action of MG with the dilaton field ϕ is defined as

$$I=\frac{1}{16\pi}\int \mathrm{d}^4x\sqrt{-g}\Big(\Re-2(\nabla\ \phi)^2-\mathrm{e}^{-2\beta\phi}F_{\mu\nu}F^{\mu\nu} + m_0^2\sum_{i=1}^{4}c_i\mathrm{e}^{\beta_i\phi}U_i(g,h)\Big), \tag{1}$$

where the dilaton scalar field is denoted by $\phi=\phi(r)$. With coupling constants of β_i, the last term manifests the non-minimal coupling between the massive graviton and the scalar field. The graviton's mass is m_0, and the dimensionless coupling coefficients are c_i. Observational constraints from gravitational wave detections by LIGO/Virgo have placed upper bounds on the graviton mass. For instance, the analysis of GW170104 and other events provides an upper limit on the graviton's Compton wavelength, translating to a graviton mass constraint of $m_g \lesssim 1.2\times10^{-22}\,\mathrm{eV}/c^2$ [47].

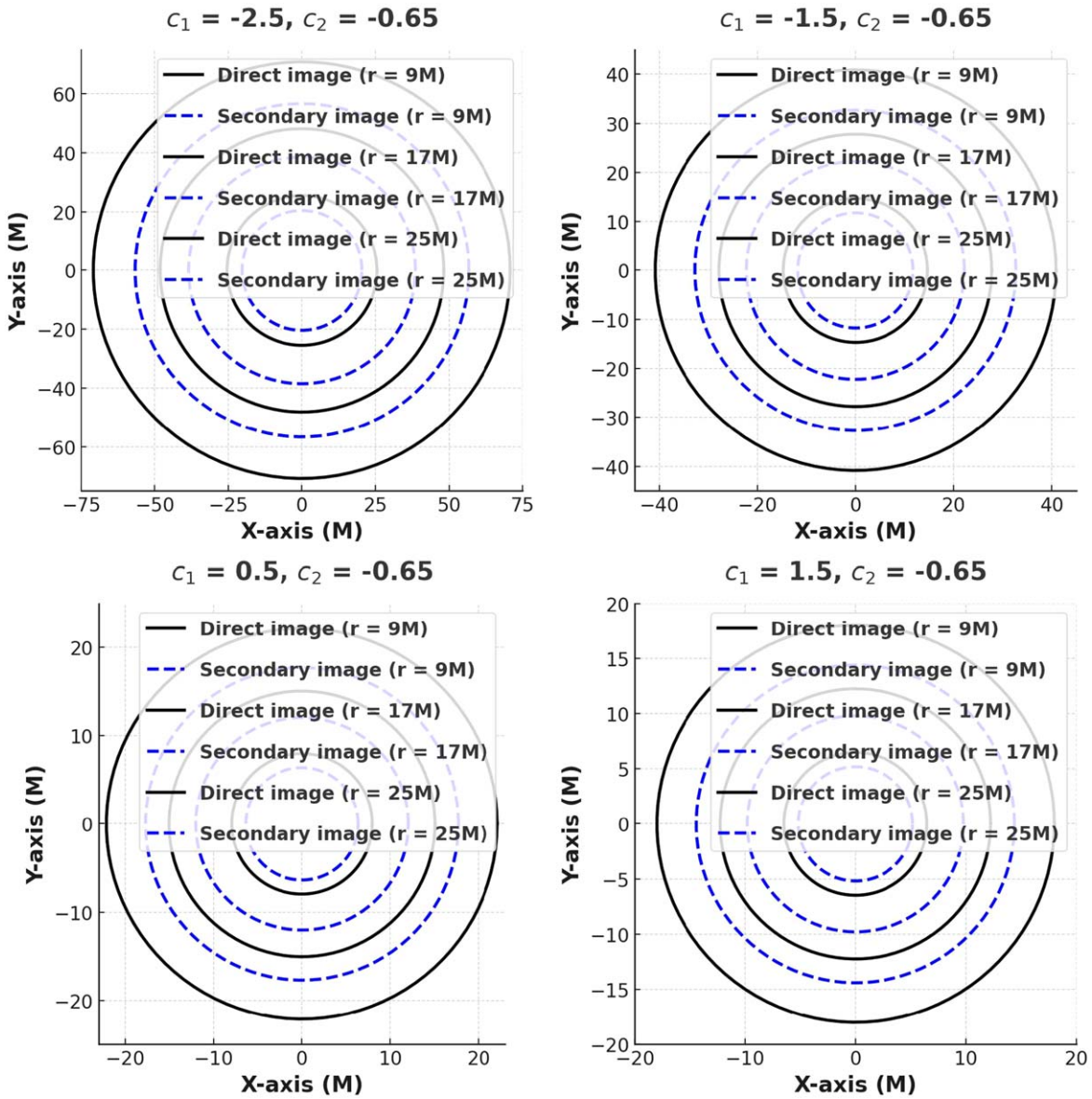

Figure 1. The plot of the images of accretion disks surrounding a dilatonic BH in dilaton-MG for different values of $c_1 = -2.5$, -1.5, 0.5, 1.5, for fixed $c_2 = -0.65$, $c_0 = 1$, $m_0 = 1$ and $M = 1.3$.

Constraining the mass of the graviton with the planetary ephemeris INPOP [48]. The symmetric polynomials U_i of the eigenvalues that satisfy the following recursion relation [49].

$$\begin{aligned} U_1 &= [K] = K^{\mu}{}_{\mu}, \\ U_2 &= [K]^2 - [K^2], \\ U_3 &= [K]^3 - 3[K][K^2] + 2[K^3], \\ U_4 &= [K]^4 - 6[K^2][K]^2 \\ &\quad + 8[K^3][K] + 3[K^2]^2 - 6[K^4]. \end{aligned} \tag{2}$$

The equations of motion are derived by varying the action with respect to $g_{\mu\nu}$ and ϕ

$$\begin{aligned} G_{\mu\nu} &= 2\mathrm{e}^{-2\beta\phi}\left[F_{\mu\lambda}F^{\lambda}{}_{\nu} - \frac{1}{4}g_{\mu\nu}F_{\lambda\rho}F^{\lambda\rho}\right] \\ &\quad + 2\partial_\mu\phi\partial_\nu\phi - (\nabla\ \phi)^2 g_{\mu\nu} + m_0^2\Xi_{\mu\nu}, \end{aligned} \tag{3}$$

$$\nabla^2\phi = -\frac{1}{4}\left[2\beta\mathrm{e}^{-2\beta\phi}F_{\lambda\rho}F^{\lambda\rho} + m_0^2\sum_{i=1}^{4}\frac{\partial\tilde{c}_i}{\partial\phi}U_i\right], \tag{4}$$

$$\nabla_\mu(\mathrm{e}^{-2\beta\phi}F^{\mu\nu}) = 0, \tag{5}$$

where

$$\tilde{c}_i = c_i\mathrm{e}^{\beta_i\phi}, \tag{6}$$

$$\begin{aligned} \Xi_{\mu\nu} &= \frac{\tilde{c}_1}{2}(-K_{\mu\nu} + U_1 g_{\mu\nu}) \\ &\quad + \frac{\tilde{c}_2}{2}(-2U_1K_{\mu\nu} + U_2 g_{\mu\nu} + 2K_{\mu\nu}^2) \\ &\quad + \frac{\tilde{c}_3}{2}(-3U_2K_{\mu\nu} + U_3 g_{\mu\nu} + 6U_1K_{\mu\nu}^2 - 6K_{\mu\nu}^3) \\ &\quad + \frac{\tilde{c}_4}{2}(U_4 g_{\mu\nu} - 4U_3K_{\mu\nu} + 12U_2K_{\mu\nu}^2 \\ &\quad - 24U_1K_{\mu\nu}^3 + 24K_{\mu\nu}^4). \end{aligned} \tag{7}$$

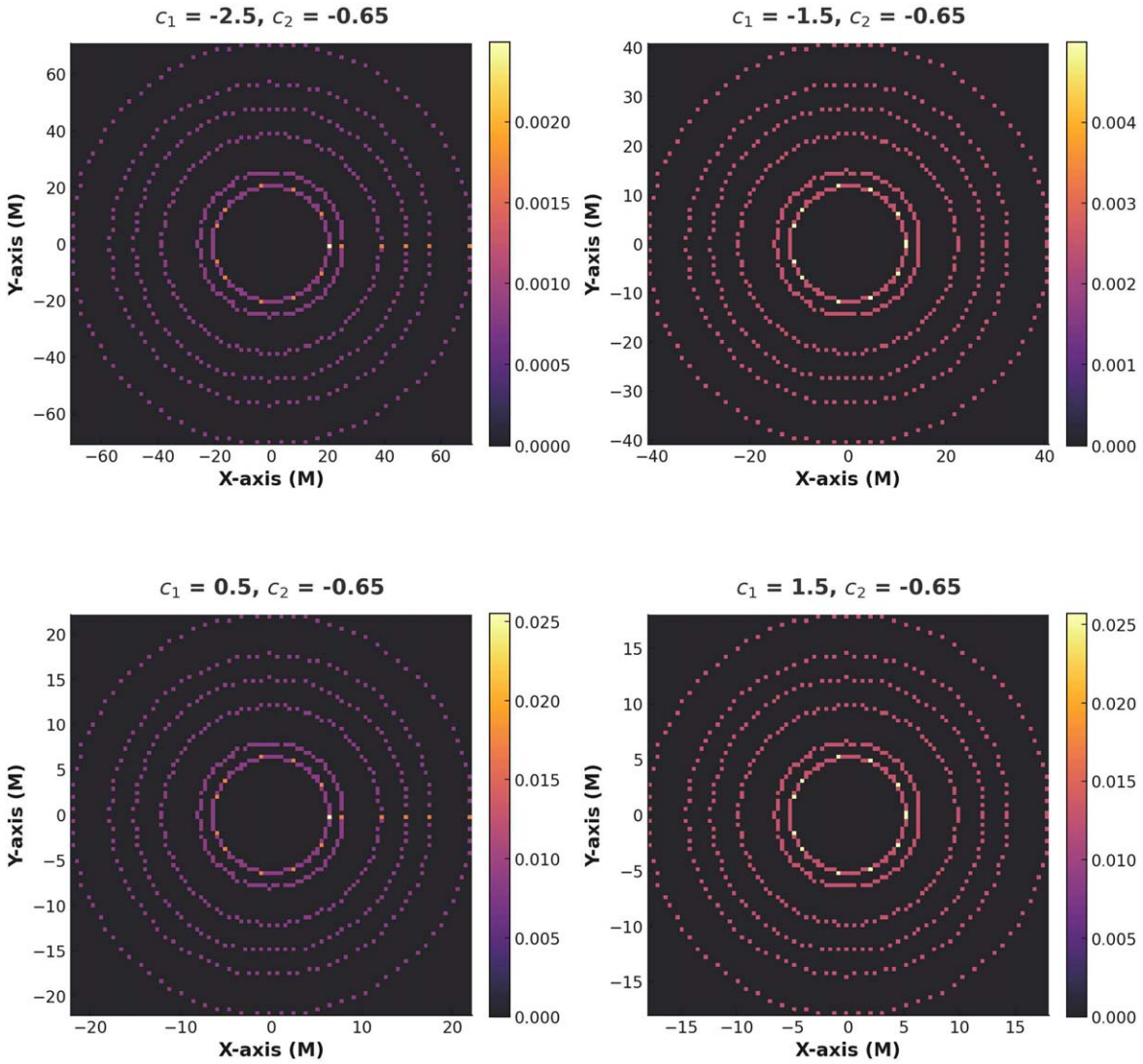

Figure 2. The density plot of the images of accretion disks surrounding a dilatonic BH in dilaton-MG for different values of $c_1 = -2.5, -1.5, 0.5, 1.5$, for fixed $c_2 = -0.65$, $c_0 = 1$, $m_0 = 1$ and $M = 1.3$.

We present the metric ansatz that is both static and spherically symmetric [50]

$$\mathrm{d}s^2 = -f(r)\mathrm{d}t^2 + \frac{\mathrm{d}r^2}{f(r)} + r^2R(r)^2\mathrm{d}\Omega^2. \tag{8}$$

Here $f(r)$ and $R(r)$ are functions of r, and $\mathrm{d}\Omega^2 = \sin^2\theta d\phi^2 + d\theta^2$ is the line element [51]. Selecting a suitable form makes the calculations easier [51]. In this study, we follow the approach in [52, 53] by defining the fiducial metric as

$$h_{\mu\nu} = \mathrm{diag}(0,\, 0,\, c_0^2,\, c_0^2\sin^2\theta). \tag{9}$$

Using the ansatz in equation (9), the interaction potential in equation (2) is modified to

$$U_1 = \frac{2c_0}{rR}, \quad U_2 = \frac{2c_0^2}{r^2R^2}, \quad U_3 = U_4 = 0. \tag{10}$$

By solving Maxwell's equation in equation (5), the electromagnetic field tensor can be expressed as

$$F_{tr} = \frac{Qe^{2\beta\phi}}{r^2R^2}, \tag{11}$$

where Q is an integration constant related with the BH's electric charge. The charged dilatonic BH in dilaton-massive gravity [50]

$$\begin{aligned} f(r) = -2Mr^{-\frac{1}{3}-\frac{4}{6+9c_0m_0^2c_1}} &+ \frac{1}{2}(2+3c_0m_0^2c_1)r^{\frac{2c_0m_0^2c_1}{2+3c_0m_0^2c_1}} \\ &+ \frac{Q^2(2+3c_0m_0^2c_1)r^{\frac{-4}{3}-\frac{4}{6+9c_0m_0^2c_1}}}{2(1+c_0m_0^2c_1)} \\ &+ \frac{c_0^2m_0^2(2+3c_0m_0^2c_1)^2c_2}{2(1+c_0m_0^2c_1)(2+c_0m_0^2c_1)}. \end{aligned} \tag{12}$$

Our findings simplify to the Schwarzschild case when $c_1 = c_2 = Q = 0$, and yields Reissner-Nordstrm case when $c_1 = c_2 = 0$. In the case of $c_1 > 0$, $f(r)$ approaches $+\infty$ as $r \to \infty$. In the case of $c_1 < -1$, $f(r)$ approaches $-\infty$ as

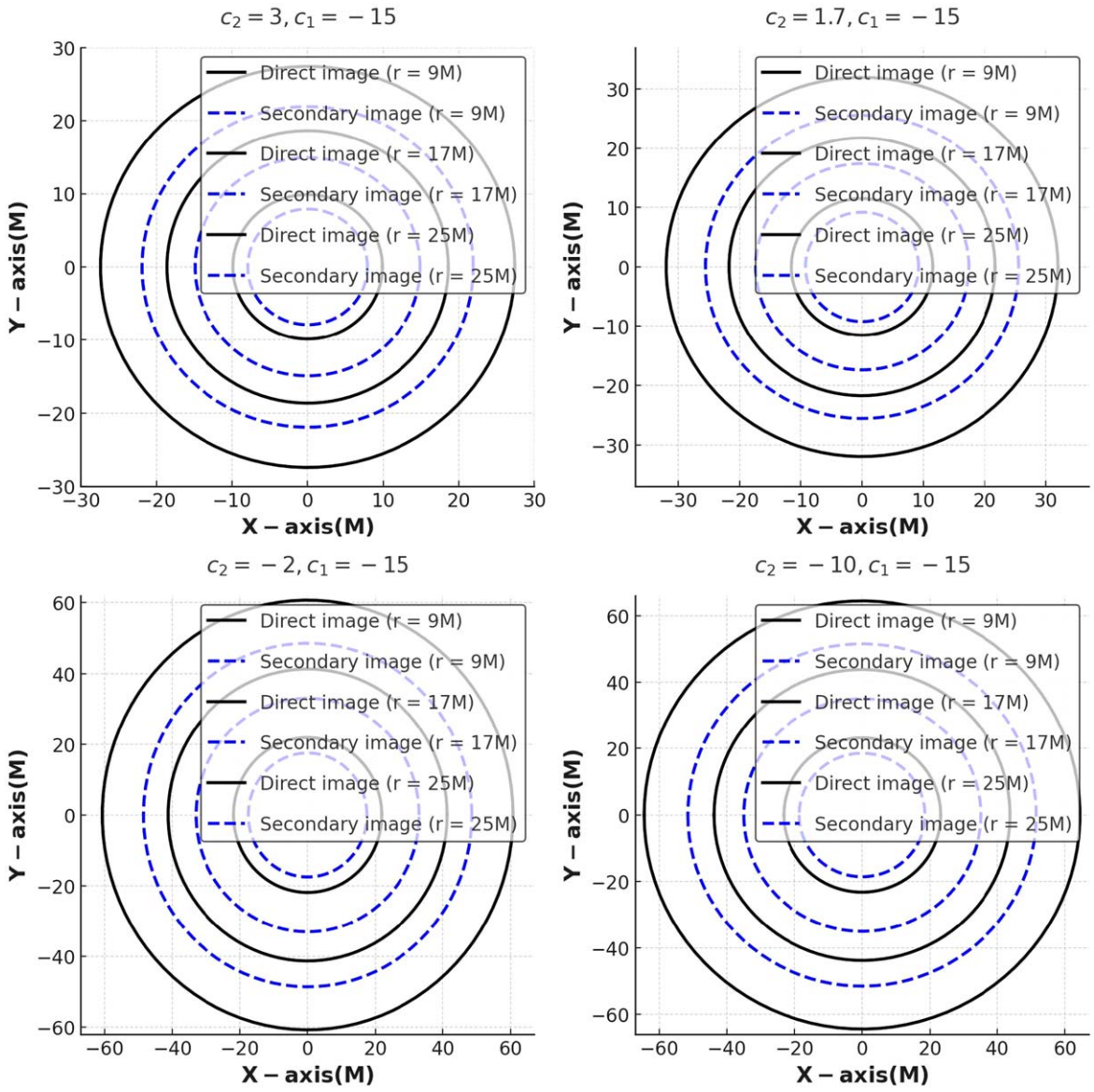

Figure 3. The plot of the images of accretion disks surrounding a dilatonic BH in dilaton-MG for different values of $c_2 = 3, 1.7, -2, -10$, for fixed $c_1 = -15$, $c_0 = 1$, $m_0 = 1$ and $M = 1.3$.

$r \to \infty$. In the next section, we examine the Novikov–Thorne model for thin accretion disks around the BH under consideration. A key requirement for the applicability of this model is that the spacetime metric must be asymptotically flat [54]. Therefore, we focus on dilatonic BHs in dilaton-massive gravity without charge $Q = 0$ which turns out to be

$$f(r) = -2Mr^{-\frac{1}{3}-\frac{4}{6+9c_0m_0^2c_1}} + \frac{1}{2}(2 + 3c_0m_0^2c_1)r^{\frac{2c_0m_0^2c_1}{2+3c_0m_0^2c_1}} + \frac{c_0^2m_0^2(2 + 3c_0m_0^2c_1)^2c_2}{2(1 + c_0m_0^2c_1)(2 + c_0m_0^2c_1)}, \quad (13)$$

which is the special case of asymptotically flat metric. For a detailed analysis of the metric function and its horizons, we refer the reader to [55], where the authors demonstrated that the parameter c_1 influences the asymptotic behavior of $f(r)$. Additionally, the parameter ranges $-1 < c_1 < 0$ and $-1 < m_0^2c_0c_1 < 0$ must be excluded. The parameters are chosen to align with theoretical constraints and ensure physical relevance within the framework of the Einstein-dilaton-MG model. For example, the values of c_1, c_2, and m_0^2 were selected to satisfy the conditions for stable BH solutions and to avoid unphysical divergences in the metric function $f(r)$. The parameters are also chosen to represent scenarios that have observable effects, such as changes in the accretion disk dynamics or gravitational lensing patterns. This ensures that the results are meaningful for potential astrophysical applications. Where applicable, we adopted parameter ranges consistent with those used in prior works on similar models (e.g., [55]) to facilitate comparison and validate our results. Now, we briefly study the geodesic motion of particles that adhere to timelike geodesics. We consider $\xi_t = \partial_t$ and $\xi_\phi = \partial_\phi$ as Killing vectors corresponding to E and L (energy

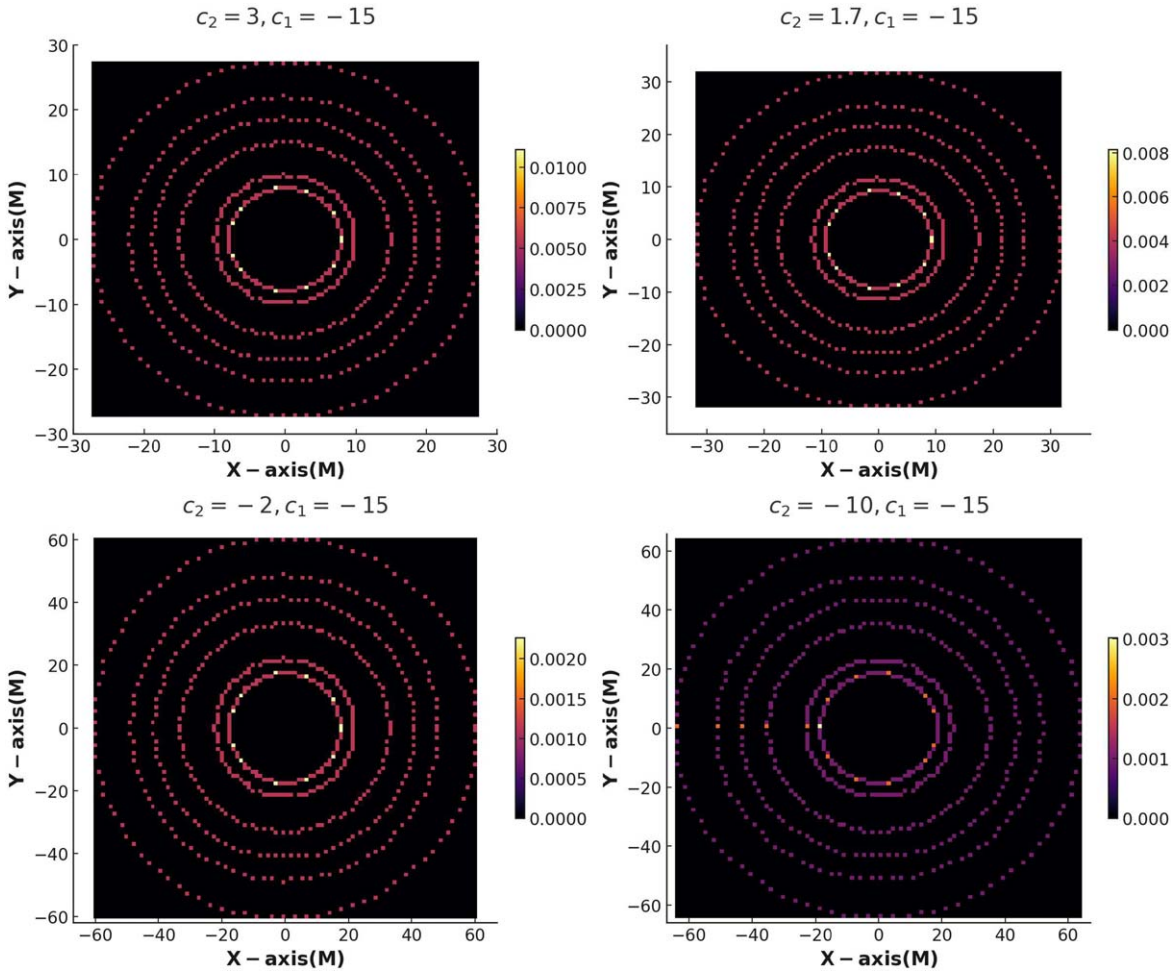

Figure 4. The density plot of the images of accretion disks surrounding a dilatonic BH in dilaton-MG for different values of $c_2 = 3$, 1.7, −2, −10, for fixed $c_1 = -15$, $c_0 = 1$, $m_0 = 1$ and $M = 1.3$.

and momentum) along the given trajectory

$$E = -g_{\mu\nu}\xi_t^{\mu}u^{\nu} \equiv -u_t, \tag{14}$$

and

$$L = g_{\mu\nu}\xi_{\phi}^{\mu}u^{\nu} \equiv u_{\phi}, \tag{15}$$

where $u^{\mu} = \frac{\mathrm{d}x^{\mu}}{\mathrm{d}\tau} = (u^t, u^r, u^{\theta}, u^{\phi})$. The four-velocity vector u^{μ} satisfies the normalization condition $u^{\mu}u_{\mu} = -1$, leading to

$$[g_{\theta\theta}(u^{\theta})^2 + g_{rr}(u^r)^2] = [1 - g^{\phi\phi}(u_{\phi})^2 - g^{tt}(u_t)^2]. \tag{16}$$

From equations (14), (15), and (16) for $\theta = \frac{\pi}{2}$, we have

$$u^t = -\frac{E}{f(r)}, \tag{17}$$

$$u^{\theta} = 0, \tag{18}$$

$$u^{\phi} = -\frac{L}{r^2}, \tag{19}$$

where $f(r)$ depends on the radial coordinate r

$$u^r = \sqrt{-f(r)\left(1 - \frac{E^2}{f(r)} + \frac{L^2}{r^2}\right)}. \tag{20}$$

Then equation (20) gives

$$(u^r)^2 + V_{\mathrm{eff}} = E^2, \tag{21}$$

where

$$V_{\mathrm{eff}} = f(r)\left(1 + \frac{L^2}{r^2}\right), \tag{22}$$

is the effective potential. The effective potential plays a crucial role in the geodesic motion of particles, as it enables the determination of the innermost stable circular orbit (ISCO) by examining its local extrema. The conditions for circular motion are

$$u^r = \frac{\mathrm{d}r}{\mathrm{d}\tau} = 0 \quad \text{and} \quad \dot{u}^r = \frac{\mathrm{d}^2r}{\mathrm{d}\tau^2} = 0. \tag{23}$$

With these two conditions and by using equation (21), one can obtain

$$V_{\mathrm{eff}} = E^2 \quad \text{and} \quad \frac{\mathrm{d}}{\mathrm{d}r}V_{\mathrm{eff}} = 0. \tag{24}$$

The Ω_{ϕ}, E and L of the particle can then be determined. The angular velocity, Ω_{ϕ}, is defined as the rate of change of the azimuthal coordinate ϕ with respect to the time coordinate t, for a particle in circular motion. Mathematically, it is

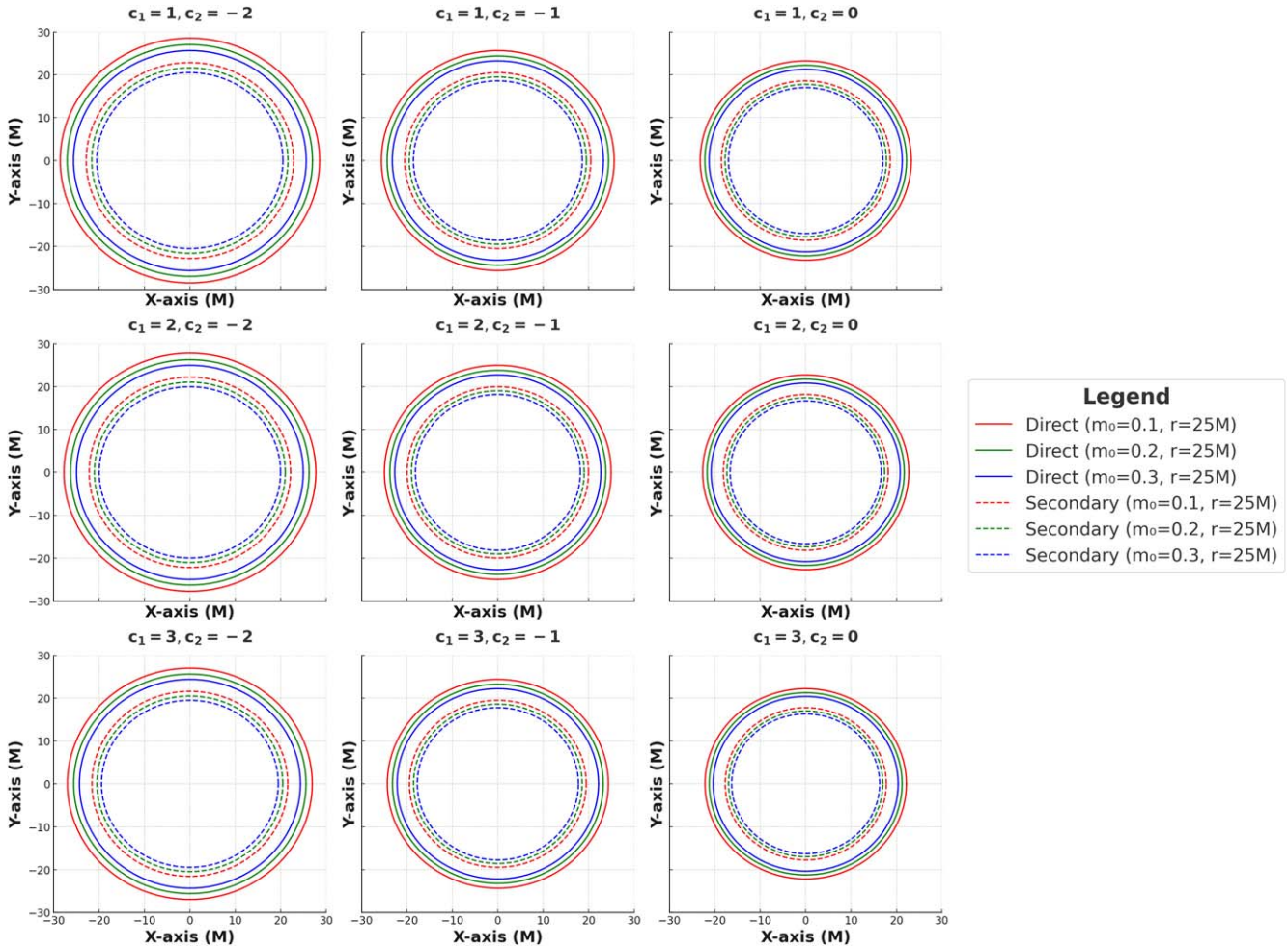

Figure 5. The plot of the images of accretion disks surrounding a dilatonic BH in dilaton-MG for different values of c_1, c_2 and m_0. Left to right plots correspond to increasing c_2 and top to bottom plots correspond to increasing c_1.

expressed as

$$\Omega_\phi = \frac{\mathrm{d}\phi}{\mathrm{d}t} = \frac{u^\phi}{u^t},$$

where u^ϕ and u^t are components of the four-velocity u^μ, which satisfies the geodesic equations of motion. From the normalization condition $u^\mu u_\mu = -1$ and the Killing symmetries of the spacetime, the energy E and angular momentum L of the particle are conserved quantities, given by

$$E = -g_{tt}u^t, \quad L = g_{\phi\phi}u^\phi.$$

For a circular orbit in the equatorial plane ($\theta = \pi/2$), substituting these relations and solving for u^ϕ/u^t, we obtain

$$\Omega_\phi = \frac{u^\phi}{u^t} = \frac{g^{tt}L}{g_{\phi\phi}E}.$$

Subsequently, for the specific metric used in the manuscript, the angular velocity simplifies to

$$\Omega_\phi^2 = \frac{1}{2r}f'(r), \tag{25}$$

$$E^2 = \frac{2f^2(r)}{2f(r) - rf'(r)}, \tag{26}$$

and

$$L^2 = \frac{r^3 f'(r)}{2f(r) - rf'(r)}. \tag{27}$$

From equations (26) and (27), E and L must be real if

$$2f(r) - rf'(r) > 0, \tag{28}$$

and $-rf'(r) + 2f(r) = 0$ allows the determination of the photon sphere radius, which is critical for studying gravitational lensing. Stable circular orbits exist when the effective potential reaches a local minimum, which occurs under the condition

$$\frac{\mathrm{d}^2 V_{\mathrm{eff}}}{\mathrm{d}r^2} > 0. \tag{29}$$

From equation (22), we have

$$\frac{\mathrm{d}^2 V_{\mathrm{eff}}}{\mathrm{d}r^2} = \left(1 + \frac{L^2}{r^2}\right)f'' - \frac{4L^2}{r^3}f' + \frac{6L^2}{r^4}f. \tag{30}$$

The radius of the ISCO, denoted as r_{ISCO}, can be determined by satisfying the conditions $V_{\mathrm{eff}} = 0$, $\frac{\mathrm{d}V_{\mathrm{eff}}}{\mathrm{d}r} = 0$, and $\frac{\mathrm{d}^2 V_{\mathrm{eff}}}{\mathrm{d}r^2} = 0$. The circular photon orbit r_{ph}, corresponds to the extreme point of the effective potential $\frac{\mathrm{d}V_{\mathrm{eff}}}{\mathrm{d}r}|_{r=r_{\mathrm{ph}}} = 0$. The condition

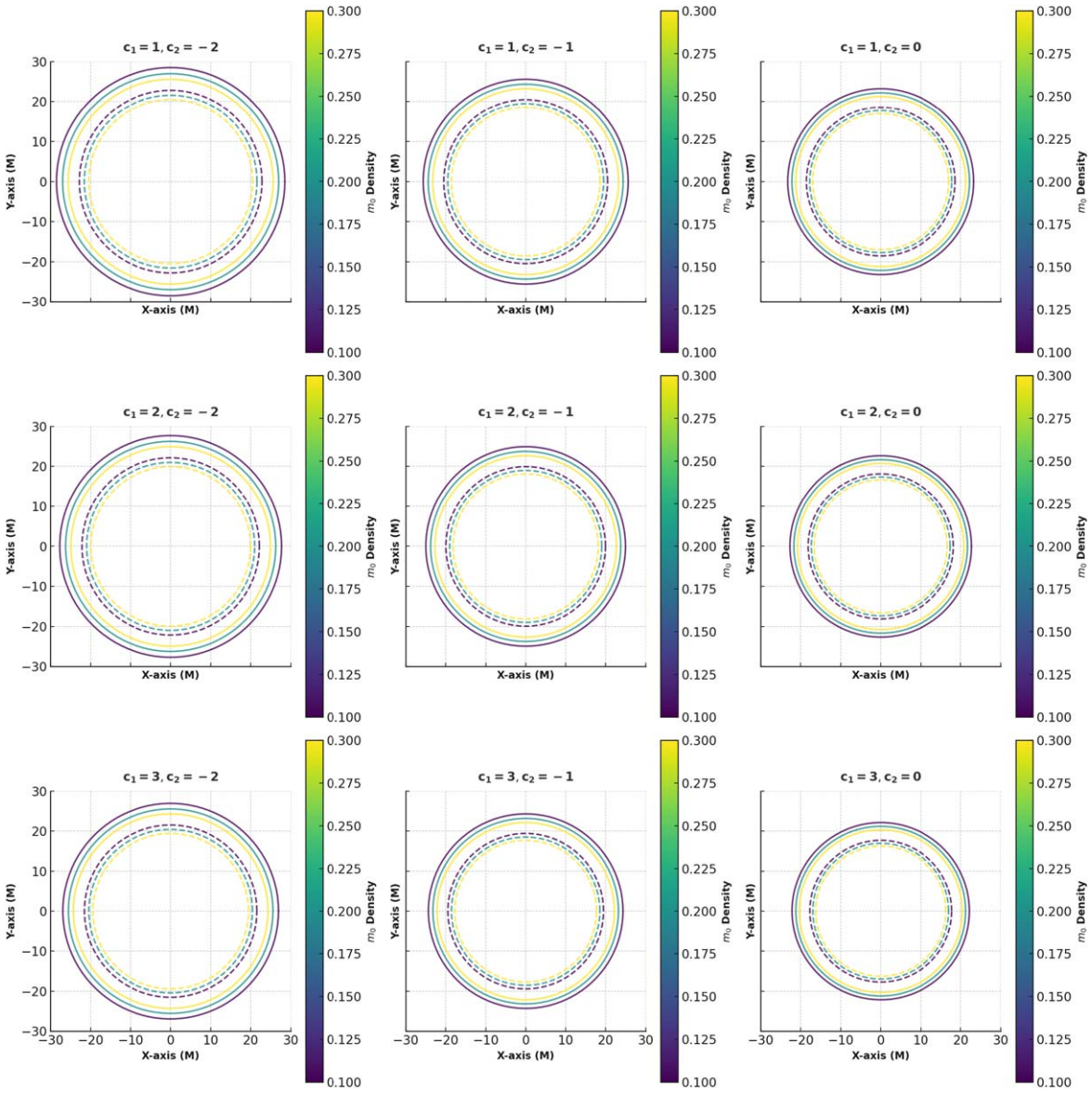

Figure 6. The density plot of the images of accretion disks surrounding a dilatonic BH in dilaton-MG for different values of c_1, c_2 and m_0. Left to right plots correspond to increasing c_2 and top to bottom plots correspond to increasing c_1.

$V_{\text{eff}} = 0$ is fundamental in the analysis of particle motion around black holes. It signifies the total energy balance of the system. Specifically in the framework of geodesic motion, the effective potential V_{eff} encapsulates the gravitational, centrifugal, and other potential contributions acting on a test particle. The equality $V_{\text{eff}} = 0$ corresponds to the threshold where the total energy E^2 equals the effective potential energy, marking the boundary between bound and unbound trajectories. For circular orbits, $V_{\text{eff}} = E^2$ holds, as it ensures that the radial velocity $u^r = \frac{\mathrm{d}r}{\mathrm{d}\tau} = 0$. The specific value of E^2 determines whether a circular orbit is possible at a given radial coordinate r. This condition is critical for determining the ISCO, where stable circular motion ceases to exist. By analyzing $V_{\text{eff}} = E^2$, along with its derivatives $\frac{\mathrm{d}V_{\text{eff}}}{\mathrm{d}r} = 0$ and $\frac{\mathrm{d}^2V_{\text{eff}}}{\mathrm{d}r^2} > 0$, the ISCO radius can be identified.

3. Analysis of the accretion disk around Dilatonic BHs in dilaton-massive gravity

A detailed overview of the Novikov–Thorne model for thin accretion disks can be found in [4]. For an observer at a specific distance, the overall change in the ray bending angle that leads to subsequent effects is expressed as [56]

$$\begin{aligned}\psi(u) &= \int_{u_{\text{source}}}^{u_{\text{obs}}} \frac{1}{\Omega(u)}\mathrm{d}u \\ &= \int_{u_{\text{source}}}^{u_{\text{obs}}} \left(\frac{1}{b^2} - u^2 f(u)\right)^{-1/2} \mathrm{d}u. \end{aligned} \tag{31}$$

Here, $u \equiv r^{-1}$. u_{source} manifests emission point of photon while u_{obs} denoted observer's position. A radial inflection point, represented by u_0, may appear when certain ray impact parameters exceed a critical value. The photon's path in this

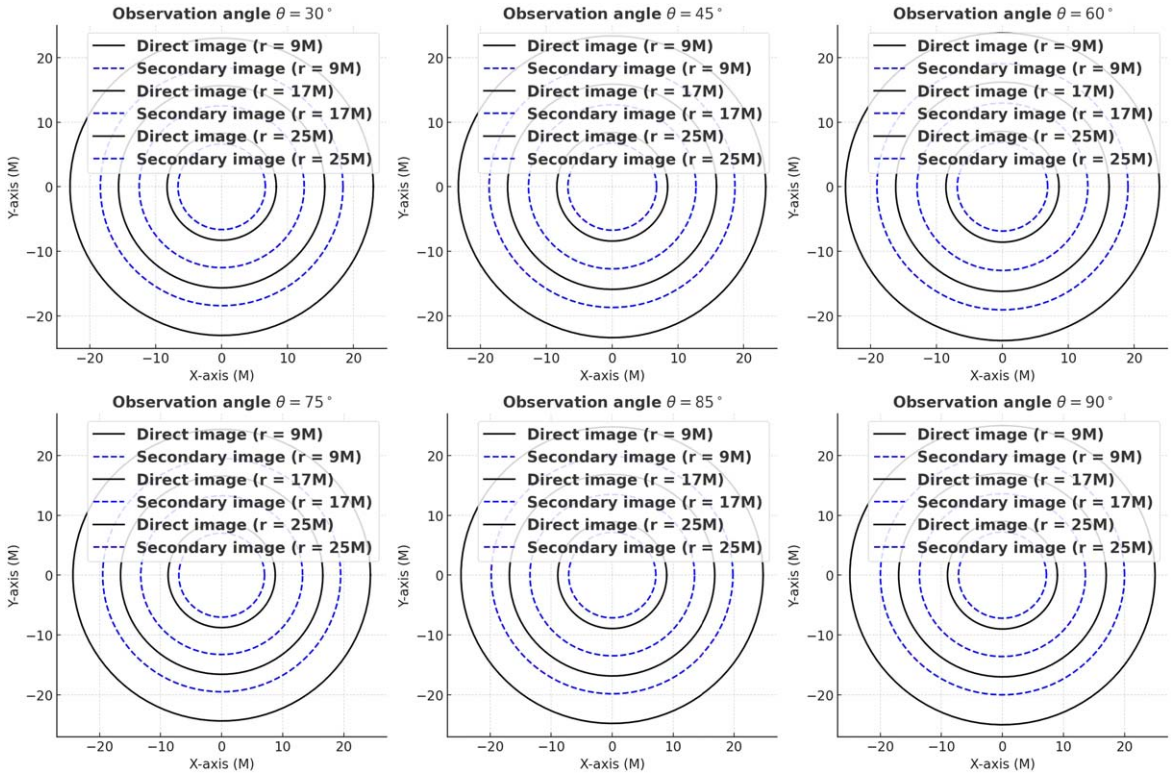

Figure 7. The plot of the images of accretion disks surrounding a dilatonic BH in dilaton-MG for different observation angles $\theta = 30^{\circ}, 45^{\circ}, 60^{\circ}, 75^{\circ}, 85^{\circ}, 90^{\circ}$. The plot correspond to $c_1 = 0.5$, $c_2 = -0.65$, $c_0 = 1$, $m_0 = 1$ and $M = 1.3$.

case can be divided into two distinct segments from u_{source} to u_0, and from u_0 to u_{obs}. The following gives the radial inflection point

$$u_0 = \frac{1}{b^2} f(r)^{-1}, \tag{32}$$

in these sections. Numerical integration methods are used to obtain primary/secondary images. The paths of the photon are obtained as follows [56]

$$\int_{u_{\text{source}}}^{u_{\text{obs}}} \left(\frac{1}{b^2} - u^2 f(u)\right)^{-1/2} \mathrm{d}u = \pi n - \cos^{-1} \times \left(\frac{1}{\sqrt{\sin^2\eta \tan^2\theta + 1}} \tan\theta \sin\eta\right), \tag{33}$$

where the celestial angle is given by η, the impact parameter is b, and the observer's tilt angle is given by θ. Here n denotes the image order, with $n = 0$ indicating the direct and $n = 1$ indicating the secondary image. The photon's trajectory is defined by the azimuthal angle η and the impact parameter b. The observer's inclination can be deduced immediately from this equation. By specifying r, the equation can be changed to represent a relationship between b and η for a specific orbit. The metric's parameters are also incorporated and treated as constants. This model helps with the understanding of how changes to these parameters affect spacetime geometry as well as the appearance of the accretion disk. It is not possible to solve for u using direct integration. However, if one limits η to the limit 0 to π, one may use a root-finding method to determine the value of b, which in turn provides the orbital image that's observed.

Figures 1 and 2 show images of the accretion disk surrounding a dilatonic BH in dilaton-MG for different values of $c_1 = -2.5$, -1.5, 0.5, and 1.5 for fixed at $c_2 = -0.65$. The accretion disk is viewed at an observation angle of 75°. The direct images, which are closer to circular, are slightly deformed as c_1 decreases and becomes negative. This suggests that the gravitational potential around the BH is modified by the dilaton-MG parameters, causing more pronounced light deflection at smaller c_1 values. The secondary images, which result from photons orbiting the BH, become increasingly distorted and displaced with lower values of c_1. At closer distances (e.g., $r = 9M$), the gravitational lensing is more pronounced, especially for lower values of c_1. This shows that the dilaton and MG effects are more significant closer to the BH, where the gravitational potential is strongest. At larger distances (e.g., $r = 25M$), the accretion disk images are less deformed, indicating that the influence of the dilaton-MG terms weakens with distance from the BH. As c_1 decreases, the BH's gravitational influence becomes more intense, particularly on the secondary images. The direct images remain more circular but still show subtle signs of deformation, indicating that the influence of c_1 extends to all light paths near the BH. The fixed value of $c_2 = -0.65$ ensures that the dilaton and massive gravity effects are present but controlled. While c_1 modifies the behavior of the gravitational potential, the varying c_1 values dominate the observed changes in the accretion disk images. Overall, we can say that increasing values of c_1 show a compress behavior

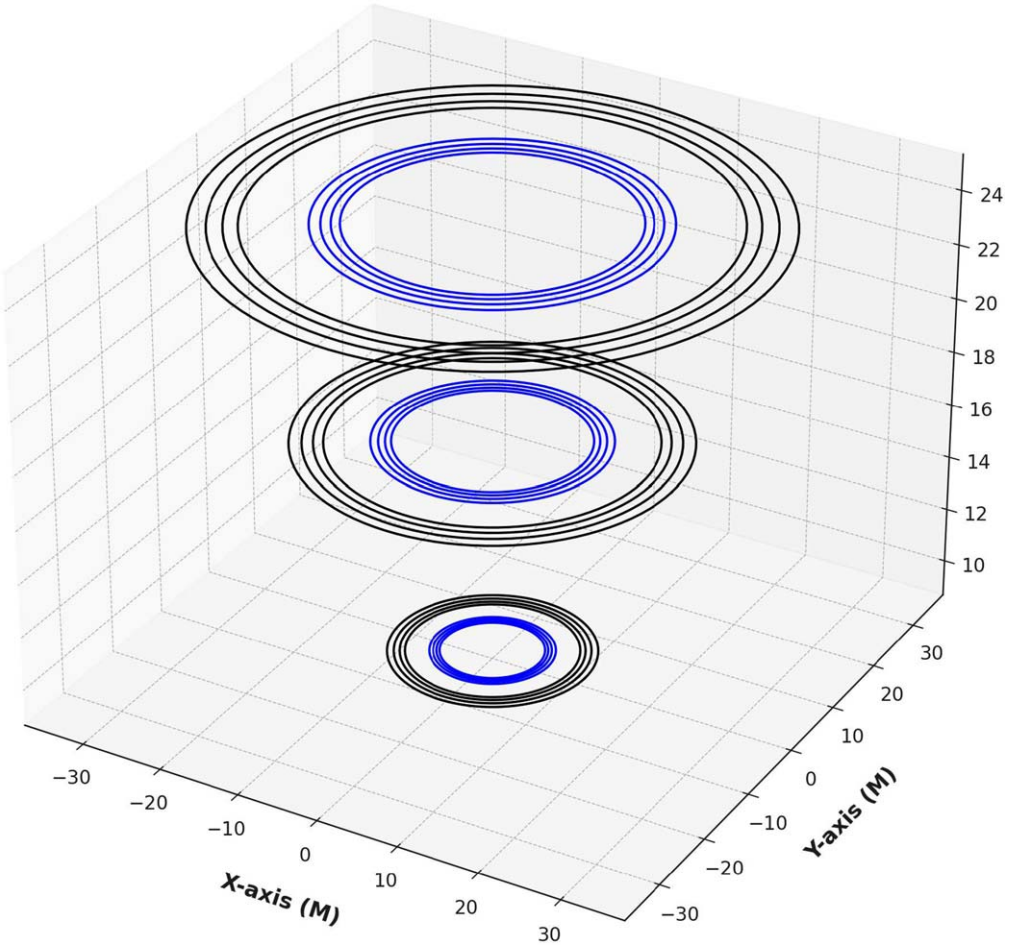

Figure 8. The 3D plot of accretion disk images of dilatonic BHs in dilaton-MG. The plot correspond to $c_1 = 0.5$, $c_2 = -0.65$, $c_0 = 1$, $m_0 = 1$ and $M = 1.3$.

in the curves. The modifications caused by the parameters c_1 and c_2 could be detected observationally through high-resolution images of BH accretion disks, such as those produced by the Event Horizon Telescope. Figure 2 shows density plots at different values of c_1 and a fixed $c_2 = -0.65$. The radial distances analyzed are $r = 9M$, $17M$, $25M$, with an observation angle of 75°. The results show that the parameters c_1 and c_2 in dilaton-MG have a significant influence on the properties of BH accretion disks. Lower values of c_1 cause stronger distortions and more intense gravitational lensing, particularly in the secondary images. The fixed value of c_2 amplifies these effects, leading to increased photon clustering around the BH. These findings suggest that by studying the accretion disk images of BHs, we can gain important insights into the nature of dilaton-MG and its effects on photon trajectories and gravitational lensing.

Figures 3 and 4 display images of the accretion disk surrounding a dilatonic BH in dilaton-MG. The values of the parameter c_2 vary across the four values $c_2 = 3$, 1.7, -2, -10 for fixed $c_1 = -15$. The parameter c_2 in dilaton-MG alters the gravitational potential around the BH, influencing how light from the accretion disk bends as it travels to the observer. As c_2 decreases from 3 to -10, the direct image distortion becomes more pronounced, with the images deviating from perfect circular shapes. This reflects the increasing curvature as c_2 decreases. The secondary images are more significantly affected, showing larger distortions and displacements at lower values of c_2. The stretched shape of the secondary images highlights the stronger gravitational lensing caused by the increased curvature due to lower c_2. The effects of gravitational lensing and distortion are most pronounced, particularly in the secondary images, which are stretched and shifted farther as c_2 decreases. The distortion is less intense, though still present, indicating that the influence of c_2 diminishes as the radial distance from the BH increases. The varying shape of the accretion disk images shows that the gravitational potential is modified by c_2. As c_2 increases, the inner regions of the disk are more heavily influenced, leading to observable distortions. Figure 4 shows density plots show the accretion disk images of dilatonic BHs in dilaton-MG, viewed at an observation angle of 75°, at ($r = 9M$, $17M$, $25M$) for different values of c_2 for fixed at $c_1 = 1$. Both the images are presented in a circular-type shape, and the color maps indicate the density of photon trajectories, where brighter regions correspond to higher photon concentrations. The parameter c_2 in dilaton-massive gravity plays a crucial role in determining the gravitational behavior of the BH and its accretion disk. Negative values of c_2 lead to stronger

gravitational lensing and more concentrated photon densities, while positive values produce weaker gravitational effects and more spread-out disk images.

Figures 5 and 6 display the images of the accretion disk surrounding a dilatonic BH in dilaton-MG, observed at an angle of 75° at distinct radial distances ($r = 9M$, $17M$, $25M$). The plots explore the impact of different values of c_2, m_0 and c_1. Direct images (solid lines) represent light rays from the accretion disk that travel relatively straight paths to the observer. Secondary images (dashed lines) represent photons that undergo gravitational lensing. The plots provide insight into how the parameters c_1, c_2 (dilatonic gravity parameters) and m_0 (MG coupling) affect the appearance of the disk. The direct images are primarily affected by potential created by the BH which is influenced by the parameters c_1 and c_2. As both c_1 and c_2 increase, the direct images exhibit more noticeable distortion. This distortion is more pronounced for higher c_1 and c_2, suggesting that the dilatonic gravity corrections strengthen the gravitational pull of the black hole, altering how light is bent in its vicinity. The secondary images, which are a result of light bending around the BH show significantly larger distortions compared to the direct images. These distortions increase with both c_1 and c_2, reflecting stronger gravitational lensing at higher values of these parameters. The direct images show a more subtle influence of m_0 indicating a slight difference in image shape for increasing m_0. The secondary images, on the other hand, show more pronounced variations with changes in m_0. As m_0 increases, the secondary images become more distorted, suggesting that larger m_0 values lead to a stronger modification of the gravitational field, enhancing lensing effects. At closer radial distances ($r = 9M$), the effects of lensing are more pronounced. The gravitational influence of the BH is stronger, leading to greater distortion. At larger distances ($r = 25M$), the gravitational effects weaken, and the images become less distorted. However, the influence of c_1, c_2 and m_0 still shows noticeable changes, albeit to a lesser extent. The changes in the accretion disk's observed shape as the parameters c_1, c_2 and m_0 vary suggest that the dynamics of the disk, including its emission characteristics, are influenced by the spacetime curvature introduced by dilaton-massive gravity. Stronger lensing effects result in a more pronounced distortion of the images, which could affect the observed intensity distribution across the disk. Figure 6 shows the density plot by showing the significant impact of the dilaton-massive gravity parameters.

Figure 7 displays images of the accretion disk surrounding a dilatonic BH in dilaton-MG for different observation angles $\theta = 30°$, $45°$, $60°$, $75°$, $85°$, $90°$. The images are formed at distinct radial distances ($r = 9M$, $17M$, $25M$). At low observation angles (e.g., 30°), the direct images appear more circular and symmetric. The gravitational lensing is less pronounced because the observer is looking at the disk from a more face-on perspective, where light deflection is minimal. As the observation angle increases to 75° and beyond, the direct images become more elliptical and deformed. The disk appears tilted as the observer views it from a more edge-on perspective, making gravitational effects more prominent. At the extreme angle of 90°, the disk is viewed edge-on, and the direct image appears as a highly elongated ellipse, reflecting the extreme warping caused by the BH's gravitational field. At low angles (e.g., 30°), the images remain relatively symmetrical. As the angle enlarges, the secondary images become more stretched and displaced. At high angles (e.g., 85° and 90°), the secondary images are dramatically elongated and warped, showing the extreme gravitational lensing experienced by light. Closer to the BH ($r = 9M$) both direct and secondary images are more strongly distorted. The gravitational lensing effects are more pronounced, particularly in the secondary images. Further from the BH ($r = 25M$) the images are less distorted, and the gravitational lensing is weaker. Both images appear circular for low observation angles, but still show elongation at higher angles. The effect of the BH's gravitational lensing becomes more pronounced as the observation angle increases. At higher angles, especially when approaching (90°), the images are significantly deformed due to the strong curvature. The edge-on view provides the clearest indication of the strong gravitational effects caused by the BH, as both images exhibit maximum distortion. The degree of lensing and distortion may also help identify specific features of the BH, such as its mass, charge, and the nature of the surrounding spacetime.

Figure 8 shows the accretion disk images of dilatonic BHs in dilaton-MG, with a focus on the parameters c_1 and c_2 influence the distortion of the images. The plot includes both direct images (in black) and secondary images (in blue) at distinct radial distances ($r = 9M$, $17M$, $25M$) and at an observation angle of 75°. As c_1 increases, the direct images exhibit more noticeable deviations from perfect circles, indicating that the modifications introduced by dilaton-MG have a stronger influence on the geometry of the accretion disk at higher values of c_1. As c_1 increases, the secondary images are stretched and bent more significantly. This suggests that higher values of c_1 lead to greater curvature effects and stronger gravitational lensing, particularly for the secondary images, which are more sensitive to gravitational perturbations. At smaller radii ($r = 9M$), the images show more pronounced distortions due to stronger gravitational effects near the BH. As the radial distance increases ($r = 25M$), the images become less distorted, as the gravitational influence weakens, and the accretion disk shapes return closer to circular forms The modification introduced by c_1 reflects the influence of MG terms in dilaton-MG, which alters the spacetime geometry around the BH. Although c_2 is fixed at -2.75 in this analysis, it also contributes to the overall distortion of the images. The combination of c_1 and c_2 determines the spacetime curvature is modified at various distances from the BH, with larger values of c_1 amplifying these effects. The differences in the direct and secondary images provide a potential observational signature for distinguishing dilaton-MG from standard general relativity. The impact of c_1 and c_2 could be tested through careful observation of accretion disks and gravitational lensing patterns around BHs. Observations of light bent near BHs could provide constraints on the values of these parameters and test the validity of dilaton-MG theories.

4. Conclusion

We have examined a newly developed BH model in Einstein-dilaton-MG, which incorporates the coupling between a

dilaton field and terms associated with a massive graviton. This model exhibits different horizon structures depending on certain parameters. To study the behavior of thin accretion disks around such BHs, we employ the widely recognized Novikov–Thorne model. Our research reveals a significant relationship between the dynamics of the accretion disk and the parameters governing dilatonic BHs in this dilaton-MG framework. We have shown the images of the accretion disk surrounding the black hole in dilaton-MG for different sets of parameters. The accretion disk is viewed at different radial distances and observation angles.

We presented the direct and secondary images displaying specific contractions and expansions for different values of the considered model. It is observed that the parameters c_1 and c_2 in dilaton-MG have an influence on the characteristics of BH accretion disks. Larger c_1 causes stronger distortions and more intense gravitational lensing, especially in the secondary images. The fixed value of c_2 increased these effects which leads to increased photon clustering around the BH. These results show that the accretion disk images of BHs provide the nature of dilaton-MG and its effects on photon trajectories and gravitational lensing.

Our study of accretion surrounding a dilatonic BH in dilaton-MG provide several astrophysical insights. The study demonstrates that potential around the BH is altered by the parameters c_1 and c_2. Lower c_1 shows stronger gravitational lensing and higher distortions, particularly in secondary images. These distortions open a new window to analyze how dilaton and MG effects alter spacetime geometry. The findings reveal that distortions are more pronounced at smaller radial distances ($r = 9M$), where spacetime curvature is stronger. At ($r = 25M$), these effects weaken, reflecting the diminishing influence of the BH's gravitational potential. By studying the gravitational lensing effects and image distortions across different radial distances and observation angles, one can investigate the interplay between dilaton fields, massive gravity, and spacetime geometry and gain insights into the microscopic structure of BHs.

Acknowledgments

The authors extend their appreciation to the Deanship of Scientific Research at Northern Border University, Arar, KSA for funding this research work through the project number NBU-FFR-2025-1102-06.

ORCID iDs

Saad Althobaiti https://orcid.org/0000-0003-2678-2066

References

[1] Akiyama K *et al* 2019 First M87 event horizon telescope results. I. The shadow of the supermassive black hole *Astrophys. J. Lett.* **875** L4

[2] Akiyama K *et al* 2022 First sagittarius A* event horizon telescope results. I. The shadow of the supermassive black hole in the center of the Milky Way *Astrophys. J. Lett.* **930** L12

[3] Shakura N I and Sunyaev R A 1973 Black holes in binary systems. Observational appearance *Astron. Astrophys.* **24** 337–55 https://inspirehep.net/literature/73651

[4] Luminet J P 1979 Image of a spherical black hole with thin accretion disk *Astron. Astrophys.* **75** 228–35

[5] Laor A 2005 Line Profiles from a Disk around a Rotating Black Hole *Astrophys. J.* **376** 205–8

[6] Gyulchev G, Nedkova P, Vetsov T and Yazadjiev S 2019 Image of the Janis–Newman–Winicour naked singularity with a thin accretion disk *Phys. Rev.* D **100** 024055

[7] Paul S, Shaikh R, Banerjee P and Sarkar T 2020 Observational signatures of wormholes with thin accretion disks *J. Cosmol. Astropart. Phys.* **2020** 055

[8] Rahaman F, Manna T, Shaikh R, Aktar S, Mondal M and Samanta B 2021 Thin accretion disks around traversable wormholes *Nucl. Phys.* B **972** 115548

[9] Liu C, Tang L and Jing J 2022 Image of the Schwarzschild black hole pierced by a cosmic string with a thin accretion disk *Int. J. Mod. Phys.* D **31** 2250041

[10] Meng K, Fan X L, Li S, Han W B and Zhang H 2023 Dynamics of null particles and shadow for general rotating black hole *J. High Energy Phys.* **11** 1–28

[11] Guo S, He K J, Li G R and Li G P 2021 The shadow and photon sphere of the charged black hole in Rastall gravity *Class. Quantum Grav.* **38** 165013

[12] Xue Y, Han J, Tu Z and Chen X 2023 Stability analysis and design of cooperative control for linear delta operator system *AIMS Math.* **8** 12671–93

[13] Kurmanov Y *et al* 2024 Accretion disks properties around regular black hole solutions obtained from non-linear electrodynamics *Phys. Dark Univ.* **46** 101566

[14] Boshkayev K, Konysbayev T, Kurmanov Y, Luongo O, Muccino M, Taukenova A and Urazalina A 2024 Luminosity of accretion disks around rotating regular black holes *Eur. Phys. J.* C **84** 230

[15] Weinberg S 1989 The cosmological constant problem *Rev. Mod. Phys.* **61** 1

[16] You L, Yang X, Wu S and Li X 2023 Finite-time stabilization for uncertain nonlinear systems with impulsive disturbance via aperiodic intermittent control *Appl. Math. Comp.* **443** 127782

[17] Ade P A *et al* 2016 Planck 2015 results. XIII. cosmological parameters *Astron. Astrophys.* **594** A13

[18] Green M B, Schwarz J H and Witten E 2012 *Superstring Theory: 25th Anniversary Edition* Vol. 1 (Cambridge: Cambridge University Press)

[19] Clement G, Galtsov D and Leygnac C 2003 Linear dilaton black holes *Phys. Rev.* D **67** 024012

[20] Yang T, Li G, Wang T, Yuan S, Yang X, Yu X and Han Q 2023 A novel 1D-convolutional spatial-time fusion strategy for data-driven fault diagnosis of aero-hydraulic pipeline systems *Math.* **11** 3113

[21] Gao C J and Zhang S N 2005 Higher-dimensional dilaton black holes with cosmological constant *Phys. Lett.* B **605** 185–9

[22] Pani P, Berti E, Cardoso V and Read J 2011 Compact stars in alternative theories of gravity: Einstein-Dilaton-Gauss–Bonnet gravity *Phys. Rev.* D **84** 104035

[23] Chaudhary S, Sultan M D, Malik A, Alanazi Y M, Jumah A B and Ashraf A 2025 Black hole optics and greybody factors in the presence of generalized Chaplygin–Jacobi dark fluid *Int. J. Theor. Phys.* **64** 1–16

[24] Torii T, Yajima H and Maeda K I 1997 Dilatonic black holes with a Gauss–Bonnet term *Phys. Rev.* D **55** 739

[25] Kanti P, Kleihaus B and Kunz J 2011 Wormholes in dilatonic Einstein–Gauss–Bonnet theory *Phys. Rev. Lett.* **107** 271101

[26] Kleihaus B, Kunz J, Mojica S and Zagermann M 2016 Rapidly rotating neutron stars in dilatonic Einstein–Gauss–Bonnet theory *Phys. Rev.* D **93** 064077
[27] Maselli A, Pani P, Gualtieri L and Ferrari V 2015 Rotating black holes in Einstein-dilaton-Gauss–Bonnet gravity with finite coupling *Phys. Rev.* D **92** 083014
[28] Ohta N and Torii T 2009 Black holes in the dilatonic Einstein–Gauss–Bonnet theory in various dimensions. III: asymptotically AdS black holes with $k = 1$ *Prog. Theor. Phys.* **121** 959–81
[29] Ohta N and Torii T 2009 Black holes in the dilatonic Einstein–Gauss–Bonnet theory in various dimensions. IV: topological black holes with and without cosmological term *Prog. Theor. Phys.* **122** 1477–500
[30] Boulware D G and Deser S 1975 Classical general relativity derived from quantum gravity *Ann. Phys.* **89** 193–240
[31] Fierz M and Pauli W E 1939 On relativistic wave equations for particles of arbitrary spin in an electromagnetic field *Proc. Roy. Soc. London Ser. A. Math. Phys. Sci.* **173** 211–32
[32] Boulware D G and Deser S 1972 Can gravitation have a finite range? *Phys. Rev.* D **6** 3368
[33] De Rham C 2014 Massive gravity-living reviews in relativity *Liv. Rev. Rel.* **17** 1–189
[34] Ghosh S G, Tannukij L and Wongjun P 2016 A class of black holes in dRGT massive gravity and their thermodynamical properties *Eur. Phys. J.* C **76** 1–15
[35] Yu M, Wu S and Li X 2023 Exponential stabilization of nonlinear systems under saturated control involving impulse correction *Nonlinear Anal.: Hybrid Syst.* **48** 101335
[36] Yang Y, Qi Q, Hu J, Dai J and Yang C 2023 Advances in digitalization and machine learning for integrated building-transportation energy systems *Fractal Fract.* **7** 760
[37] Acea, A, Lpez, E and Llerena, M 2018 Isoperimetric surfaces and area-angular momentum inequality in a rotating black hole in new massive gravity *Phys. Rev.* D **97** 064043
[38] Hendi S H and Momennia M 2019 Thermodynamic description and quasinormal modes of adS black holes in Born-Infeld massive gravity with a non-abelian hair *J. High Energy Phys.* JHEP2019(2019)1
[39] Ali F, Afsar H, Alshamrani A, Sheraz M, Chee Chuah T and Loong Lee Y 2024 Improving optical transmission performance in multi-channel networks utilizing convolutional neural network-enabled digital signal processing to mitigate four *Fibre Integr. Opt.* **43** 261–82
[40] Gao C J and Zhang S N 2004 Dilaton black holes in the de Sitter or anti-de Sitter universe *Phys. Rev.* D **70** 124019
[41] Hendi S H, Faizal M, Panah B E and Panahiyan S 2016 Charged dilatonic black holes in gravity's rainbow *Eur. Phys. J.* C **76** 1–15
[42] Martinovic K and Sakellariadou M 2019 Constraints on quasidilaton massive gravity *Phys. Rev.* D **100** 124016
[43] Rezaei Akbarieh A, Kazempour S and Shao L 2021 Cosmological perturbations in Gauss–Bonnet quasi-dilaton massive gravity *Phys. Rev.* D **103** 123518
[44] Abishev M E, Boshkayev K A and Ivashchuk V D 2017 Dilatonic dyon-like black hole solutions in the model with two Abelian gauge fields *Eur. Phy. J.* C **77** 1–10
[45] Malybayev A N, Boshkayev K A and Ivashchuk V D 2021 Quasinormal modes in the field of a dyon-like dilatonic black hole *Eur. Phys. J.* C **81** 475
[46] Boshkayev K, Suliyeva G, Ivashchuk V and Urazalina A 2024 Circular geodesics in the field of double-charged dilatonic black holes *Eur. Phys. J.* C **84** 19
[47] Abbott B P *et al* 2017 GW170104: observation of a 50-solar-mass binary black hole coalescence at redshift 0.2 *Phys. Rev. Lett.* **118** 221101
[48] Bernus L, Minazzoli O, Fienga A, Gastineau M, Laskar J and Deram P 2019 Constraining the mass of the graviton with the planetary ephemeris INPOP *Phys. Rev. Lett.* **123** 161103
[49] Hinterbichler K 2012 Theoretical aspects of massive gravity *Rev. Mod. Phys.* **84** 671–710
[50] Zhang L, Pan Q, Liu B, Zhang M and Zou D C 2024 Charged dilatonic black holes in dilaton-massive gravity *Phys. Rev.* D **110** 064007
[51] Vegh D 2013 Holography without translational symmetry arXiv:1301.0537
[52] Cai R G, Hu Y P, Pan Q Y and Zhang Y L 2015 Thermodynamics of black holes in massive gravity *Phys. Rev.* D **91** 024032
[53] Xu J, Cao L M and Hu Y P 2015 P-V criticality in the extended phase space of black holes in massive gravity *Phys. Rev.* D **91** 124033
[54] Bambi C 2017 *Handbook of Gravitational Wave Astronomy* Vol. 10 (Berlin: Springer) 978–81
[55] Zhang L, Pan Q, Liu B and Zou D C 2024 Dilatonic black holes in dRGT massive gravity *Phys. Lett.* B **857** 138994
[56] Huang Y X, Guo S, Liang Y, Cui Y H, Jiang Q Q and Lin K 2024 Rastall gravity: accretion disk image in the context of radiation fields and visual transformations compared to Reissner-Nordstrm black hole *Chin. Phys.* C **48** 045102